ACS APPLIED MATERIALS & INTERFACES

www.acsami.org

Research Article

Conductive MOF on ZIF-Derived Carbon Fibers as Superior Anode in Sodium-Ion Battery

Hongmei Dai, Yue Xu,* Yongchao Han, Shixiong Sun, Xiaolin Zhang, Fangyu Xiong, Chao Huang, Chun Fang,* Jiantao Han, and Paul K. Chu

Cite This: *ACS Appl. Mater. Interfaces* 2023, 15, 29170−29177

Read Online

ACCESS | Metrics & More | Article Recommendations | Supporting Information

ABSTRACT: Superior specific capacity, high-rate capability, and long-term cycling stability are essential to anode materials in sodium-ion batteries, and conductive metal−organic frameworks (cMOF) with good electronic and ionic conductivity may satisfy these requirements. Herein, conductive neodymium cMOF (Nd-cMOF) produced *in situ* on the zeolitic imidazolate framework (ZIF)-derived carbon fiber (ZIF-CFs) platform is used to synthesize the Nd-cMOF/ZIF-CFs hierarchical structure. Four types of ZIFs with different pore diameters are prepared by electrospinning. In this novel structure, ZIF-CFs provide the electroconductivity, flexible porous structure, and mechanical stability, while Nd-cMOF provides the interfacial kinetic activity, electroconductivity, ample space, and volume buffer, consequently giving rise to robust structural integrity and excellent conductivity. The sodium-ion battery composed of the Nd-cMOF/ZIF-10-CFs anode has outstanding stability and electrochemical properties, such as a specific capacity of 480.5 mAh g^{-1} at 0.05 A g^{-1} as well as capacity retention of 84% after 500 cycles.

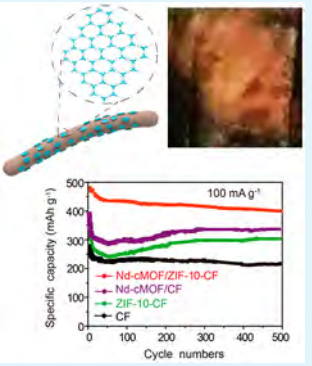

KEYWORDS: *Conductive MOFs, ZIF-derived carbon fibers, anode, interfacial kinetics, sodium-ion batteries*

INTRODUCTION

Sodium-ion batteries (SIBs) are attractive owing to the low cost and abundance of Na compared to lithium,[1−5] and electrodes with a high capacity and long-term cycling characteristics are key to the development of SIBs. However, owing to the sluggish Na^+ insertion/extraction efficiency, it is a great challenge to fulfill the increasing demand for the rate capability and specific capacity.[6−10] Much effort has been devoted to designing anode materials for sodium-ion batteries.[11−17] Unfortunately, metal alloy anodes suffer from pulverization during alloying/dealloying, leading to detachment of the active materials and deteriorated cyclability.[18−20] Transition metal sulfides are often plagued by low electronic conductivity, relatively high working potential, and large hysteresis of discharging/charging voltages, which adversely affect the energy density and efficiency.[21−23] Silicon anodes have disadvantages such as small surface area, slow charge transfer kinetics, and low electron conductivity,[24,25] and hard carbon materials are hampered by the low capacity and inferior Coulombic efficiency.[26−28] Therefore, it is still an enormous challenge to design desirable anode materials for sodium-ion batteries.

Metal−organic frameworks (MOFs) which offer adjustable pore size, versatile functionality, and large surface area are suitable for applications such as separation,[29,30] energy storage,[31,32] sensing,[33,34] and release of guest molecules.[35,36] In particular, conductive MOFs (cMOFs) have high electrical conductivity and porosity,[37−39] which bode well for anode materials in SIBs owing to the tunable structure, abundant reaction sites, and ample voids to buffer the volume change. However, cMOFs-based electrodes have low mechanical strength and the synthesis is complex. Depositing cMOF on a robust substrate is a viable strategy, and porous carbon materials for the formation of ZIF precursors can provide the optimal and flexible porous structure with mechanical stability. The pore size of carbon can be adjusted by selecting a ZIF with the proper size, and so ZIF-derived carbon fibers can improve the mechanical strength of cMOFs.[40]

Herein, a new cMOF is designed and fabricated with Nd (Ln atom) and 2,3,6,7,10,11-hexaaminotriphenylene (HATP) as the building block. The f-orbitals of Ln atoms participate in bonding and electronic delocalization[41−44] to enhance the electronic conductivity (delocalization and itinerant of electrons improving the conductivity) and stability.[45,46] The cMOF is prepared on the surface of ZIF-CFs with ample and flexible pores to produce Nd-hierarchical cMOF/ZIF-CFs (Figure 1A). ZIF-1, ZIF-3, ZIF-10, and ZIF-70 with pore diameters of 0.69, 0.82, 1.2, and 1.4 nm are mixed individually with polyacrylonitrile (PAN) to fabricate ZIF-derived carbon

Received: March 27, 2023
Accepted: May 24, 2023
Published: June 9, 2023

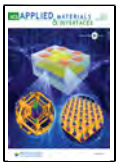

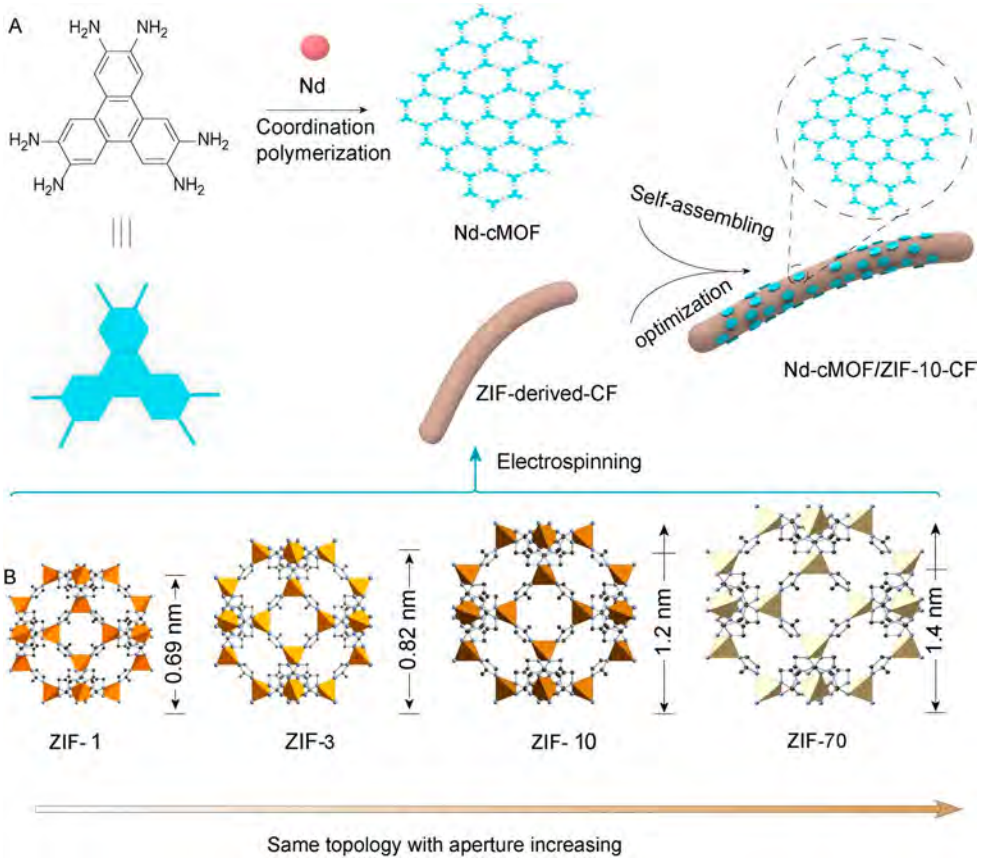

Figure 1. Schematic illustration of the synthesis of the Nd-cMOF/ZIF-CFs hierarchical structure: (A) self-assembling of Nd-cMOF on the ZIF-10-CF surface; (B) a series of ZIFs with the same topographical features.

fibers denoted as Nd-cMOF/ZIF-1-CF, Nd-cMOF/ZIF-3-CF, Nd-cMOF/ZIF-10-CF, and Nd-cMOF/ZIF-70-CF. The Nd-cMOF/ZIF-10-CF anode show the best properties, such as a specific capacity of 450.3 mAh g^{-1} at 100 mA g^{-1} as well as retention of 84% after 500 cycles.

EXPERIMENTAL SECTION

All the chemicals were purchased directly and used without further purification. Neodymium trichloride hexahydrate ($NdCl_3{\cdot}6H_2O$, Sinopharm Chemical Reagent Co., Ltd., 99.0%), 2,3,6,7,10,11-hexaiminotriphenylene hexahydrochloride (HATP·6HCl, Jilin Chinese Academy of Sciences-Yanshen Technology Co., Ltd., 99.0%), triethylamine ($(C_2H_5)_3N$, Sinopharm Chemical Reagent Co., Ltd., 99.0%), zinc nitrate hexahydrate ($Zn(NO_3)_2{\cdot}6H_2O$, Sinopharm Chemical Reagent Co., Ltd., 99.0%), imidazole (H-IM, Sinopharm Chemical Reagent Co., Ltd., 99.0%), 2-nitroimidazole ($C_3H_3N_3O_2$, Sinopharm Chemical Reagent Co., Ltd., 99.0%), N,N-dimethylformamide (DMF, Sinopharm Chemical Reagent Co., Ltd., 99.0%), 1-methyl-2-pyrrolidinone (NMP, Sinopharm Chemical Reagent Co., Ltd., 99.0%), methanol, and acetone were purchased from China National Medicines Corporation Ltd. Polyacrylonitrile (PAN, Mw = 230,000) was supplied by Aladdin Chemical Reagent Ltd.

Synthesis of Nd-cMOF. 6.0 mg of $NdCl_3{\cdot}6H_2O$, 10.0 mg of HATP·6HCl, and 15.0 mL of deionized water were mixed in a 20 mL Pyrex vial, and 0.5 mL of triethylamine was added dropwise. The mixture was heated for 4 days at 85 °C, centrifuged, and washed in deionized water. Afterward, the product was refluxed in acetone for another 2 h and vacuum-dried at 60 °C.

Synthesis of ZIFs. ZIF-1 was synthesized according to a protocol described in the literature.[47] Briefly, $Zn(NO_3)_2{\cdot}4H_2O$ (90 mg, 0.344 mmol) and H-IM (150 mg, 2.2 mmol) were dissolved in 18 mL of DMF in a 20 mL glass bottle. The mixture was heated in an autoclave at 85 °C for 24 h to yield a colorless precipitate. The product was washed with fresh DMF 3 times and dried in air.

ZIF-3 was synthesized as described previously.[48] $Zn(NO_3)_2{\cdot}4H_2O$ (10 mg, 0.0382 mmol) and H-IM (30 mg, 0.441 mmol) were dissolved in a solution of DMF (3 mL) and NMP (1 mL). The mixture was heated to 85 °C for 4 h. The crude product was purified with DMF 3 times and vacuum-dried at 120 °C for 12 h to form the activated ZIF-3.

ZIF-10 was synthesized as described previously.[49] Briefly, $Zn(NO_3)_2{\cdot}4H_2O$ (10 mg, 0.0382 mmol) and H-IM (30 mg, 0.441 mmol) were dissolved in 3 mL of DMF in a 4 mL vial and heated to 85 °C for 4 d in an autoclave to form small crystals. After cooling naturally to room temperature, the suspension was washed with a mixture of deionized water and ethanol three times and dried.

ZIF-70 was synthesized as described in the literature with slightly modification.[50] $Zn(NO_3)_2{\cdot}4H_2O$ (0.45 g), 2-nitroimidazole (5.5 g), and imidazole (5.5 g) were mixed and stirred at room temperature, capped, and heated to 110 °C for 4 days. The powders were washed with DMF (3 × 30 mL), immersed in ethanol for 3 days, and then vacuum-dried at room temperature for 12 h.

Preparation of ZIF-Derived Carbon Films (ZIF-CFs). Carbon film was synthesized through electrospinning steps as described in previous literature.[51] A mixture of ZIF powder (0.6 g) and PAN (0.2 g) were dispersed in 3 mL of DMF and stirred for 3 h. In addition, the remaining PAN (0.2 g) was added to form a uniform mixed ZIF/PAN solution with 60 wt % ZIF load. The ZIF/PAN solution was electrospun onto the aluminum foil substrates at 12 kV. The flow rate was conducted at 1 mL/h, and the spinneret diameter was 0.6 mm. The distance between the collector and spinneret was maintained at 15 cm. In the preparation of ZIF-CF film for the sodium-ion battery, the spinneret was shifted at a speed of 200 mm/min with a span of 40 mm to form a uniform layer on the aluminum foil support. The electrospinning time was 120 min.

https://doi.org/10.1021/acsami.3c04341
ACS Appl. Mater. Interfaces 2023, 15, 29170−29177

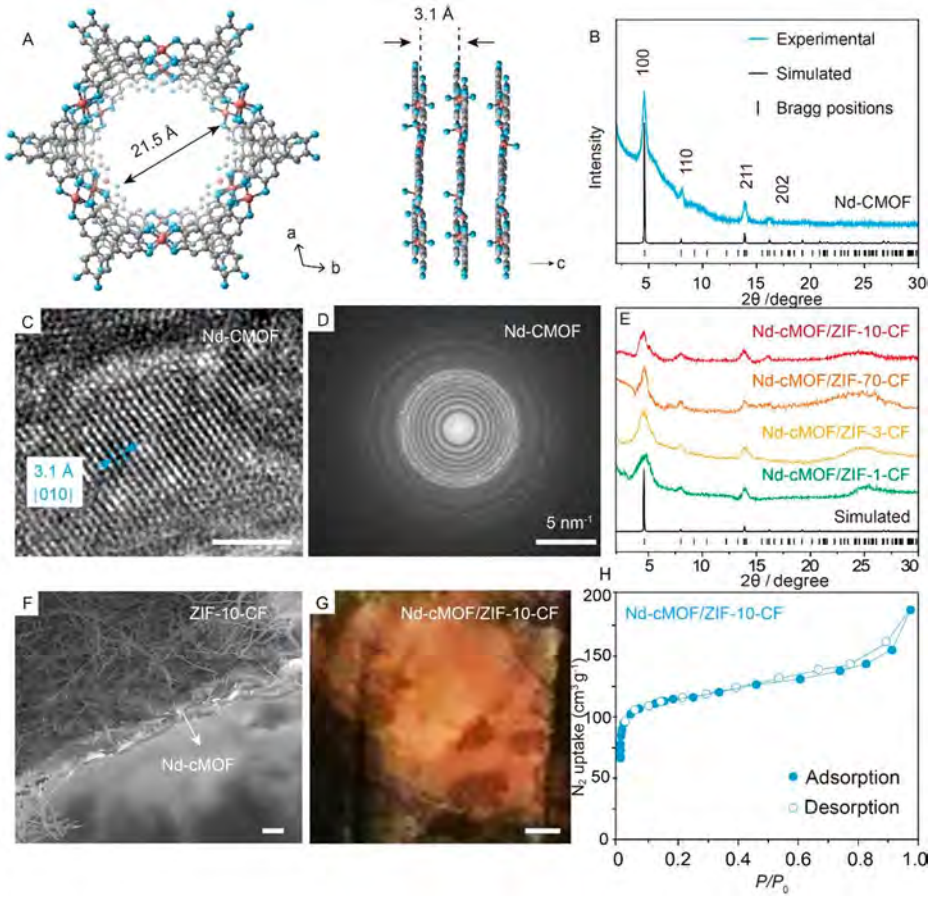

Figure 2. (A) Structure of Nd-cMOF displaying the crystallographic pore diameter (left) and layer stacking (right: Black, C; navy blue, N; light salmon, Nd. Hydrogen atoms are omitted for clarity; (B) PXRD pattern of Nd-cMOF; (C) HR-TEM image of Nd-cMOF/ZIF-10-CF, scale bar, 3 nm; (D) Electron diffraction pattern of Nd-cMOF; (E) PXRD patterns of Nd-cMOF/ZIF-10-CF (red), Nd-cMOF/ZIF-70-CF (orange), Nd-cMOF/ZIF-3-CF (yellow), and Nd-cMOF/ZIF-1-CF (green); (F) SEM image of Nd-cMOF/ZIF-10-CF, scale bar, 500 nm; (G) Image of Nd-cMOF/ZIF-10-CF, scale bar, 2 μm; (H) N_2 isotherm of Nd-cMOF/ZIF-10-CF at 77 K. The solid and open symbols represent the adsorption and desorption balance, respectively.

The ZIF-CF nanofibers were put on the aluminum foil and dried in vacuum at 70 °C for 24 h. The films were heated in air at 220 °C for 1 h and then at 1200 °C for 5 h under flowing argon. The carbon films were cropped into 12 mm diameter round electrodes for electrochemical performance test.

Synthesis of Nd-cMOF/ZIF-10-CF. ZIF-10-CF (150 mg) fibers were added into a 15 mL mixture of $NdCl_3{\cdot}6H_2O$ (6.0 mg), HATP·6HCl (10.0 mg), and triethylamine (0.5 mL) in a Pyrex bulb. The reactants were heated to 85 °C for 4 days to form Nd-cMOF/ZIF-10-CF. The product was rinsed with methanol several times until the solution was clear and then dried at 60 °C. The synthesis steps of Nd-cMOF/CF were the same as those described above except that ZIF-10-CF was replaced by CF.

Synthesis of Nd-cMOF/ZIF-1-CF. ZIF-1-CF (150 mg) fibers were immersed into a 15 mL solution containing $NdCl_3{\cdot}6H_2O$ (6.0 mg), HATP·6HCl (10.0 mg), and triethylamine (0.5 mL) in a vial. The raw materials were heated to 85 °C for 4 days to generate Nd-cMOF/ZIF-1-CF. The produced was rinsed with methanol several times until the solution was clear and then dried at 60 °C.

Synthesis of Nd-cMOF/ZIF-3-CF. ZIF-3-CF (150 mg) fibers were added into a 15 mL mixture containing $NdCl_3{\cdot}6H_2O$ (6.0 mg), HATP·6HCl (10.0 mg), and triethylamine (0.5 mL) in a Pyrex glass bottle. The crude materials were heated to 85 °C for 4 days to form Nd-cMOF/ZIF-3-CF. The product was rinsed with methanol several times until the solution was clear and then dried at 60 °C.

Synthesis of Nd-cMOF/ZIF-70-CF. Mix ZIF-70-CF (150 mg) fibers with $NdCl_3{\cdot}6H_2O$ (6.0 mg), HATP·6HCl (10.0 mg), and triethylamine (0.5 mL) in a 15 mL solution in a Pyrex vial. The mixture was heated to 85 °C for 4 days to form Nd-cMOF/ZIF-70-CF. The produced was rinsed with methanol several times until the solution was clear and then dried at 60 °C.

Synthesis of Nd-cMOF/CF. The synthesis steps of Nd-cMOF/CF were the same as those described above except that ZIF-X-CF was replaced by CF.

Synthesis of CF. 0.50 g of PAN was added into 3 mL of DMF and stirred for 3 h to form a uniformly dispersed PAN solution. The PAN solution was electrospun onto the aluminum foil substrates at a voltage of 12 kV. The flow speed was executed at 1 mL/h, while the spinneret diameter was set at 0.6 mm. The distance between the collector and spinneret was maintained at 15 cm. In the preparation of CF film for the sodium-ion battery, the spinneret was shifted at a speed of 200 mm/min with span of 40 mm to form a uniform layer on the nonwoven support. The electrospinning time was 120 min.

Electrochemical Characterization. To evaluate the electrochemical properties, the Nd-cMOF/ZIF-CFs served as the self-standing working electrode. In the CR2023 coin-type half-cell, a sodium foil was the counter electrode and 1 M $NaPF_6$ in a 50:50 (w/w) mixture of ethylenecarbonate and diethylcarbonate with 5% fluoroethylene carbonate was the electrolyte. The Whatman GF/F glass fiber membrane was the separator, and the test was conducted in an argon glovebox. The rate capability was determined at rates of 0.05, 0.2, 1, 5, and 10 Ah g^{-1} at 25 °C. Cyclic voltammetry (CV) was carried out among 0 and 3 V, and electrochemical impedance spectroscopy (EIS) was executed for different cycles at frequencies from 0.01 Hz to 100 kHz on a Princeton electrochemical workstation. $Na_3V_2(PO_4)_3$ was the active material in the cathode for the full-cell.

https://doi.org/10.1021/acsami.3c04341
ACS Appl. Mater. Interfaces 2023, 15, 29170−29177

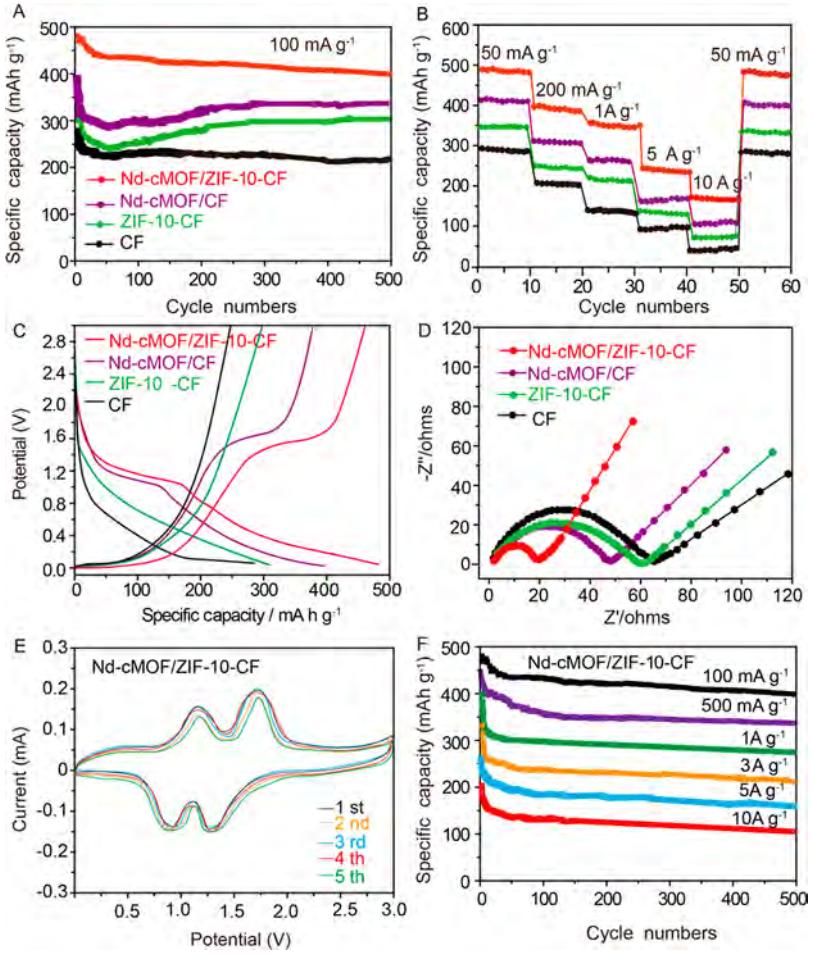

Figure 3. (A) Cyclic stability of the Nd-cMOF/ZIF-10-CF (red), Nd-cMOF/CF (purple), ZIF-10-CF (green), and CF (black) electrodes; (B) rate capabilities of Nd-cMOF/ZIF-10-CF (red), Nd-cMOF/CF (purple), ZIF-10-CF (green), and CF (black) electrode; (C) initial discharging−charging curves of the Nd-cMOF/ZIF-10-CF (red), Nd-cMOF/CF (purple), ZIF-10-CF (green), and CF (black) electrodes after 500 cycles at a current density of 100 mAg^{-1}; (D) impedance plots of Nd-cMOF/ZIF-10-CF (red), Nd-cMOF/CF (purple), ZIF-10-CF (green), and CF (black); (E) CV curves of the Nd-cMOF/ZIF-10-CF electrode for the first five cycles; (F) cycling properties of the Nd-cMOF/ZIF-10-CF electrode at different rates.

The three components of $Na_3V_2(PO_4)_3$, super P, and PVDF dissolved in NMP solution were mixed with a mass ratio of 7:2:1. The slurry was coated on copper foil and then dried overnight to obtain the electrode plate to form the cathode with an active mass loading of 1−2 mg cm^{-2}.

Instruments and Methods. The powder X-ray diffraction (XRD) patterns were tested on a Rigaku Smartlab using Cu Kα radiation (45 kV, 40 mA) at room temperature with a scanning rate of 4°/min. High resolution transmission electron microscopy (HRTEM) images were obtained on the JEM-2010F field-emission TEM equipped with a CEOS postspecimen spherical aberration corrector (CS corrector) at 120 kV. Infrared (IR) spectroscopy was performed on the Nicolet NEXUS670 IR, and the SEM images were collected on the JEOL JSM-6701F scanning electron microscope with the SEI and LEI detectors at 5−10 kV. The elemental distributions were determined by energy-dispersive X-ray spectrometry (EDS), and thermogravimetric analysis (TGA) was performed on the TA Instruments Q-500 series thermal gravimetric analyzer at a constant heating rate of 12 °C/min. The N_2 sorption isotherms were executed on the surface area and pore size analyzer (Quantachrome Autosorb-1) after the sample was degassed under vacuum atmosphere at 100 °C for 24 h.

RESULTS AND DISCUSSION

cMOF (Nd-cMOF) with a pore diameter of 21.5 Å and layer stacking of 3.0 Å is prepared (Figure 2A) by a reported protocol with minor modification.[52] The f-orbitals of Ln atoms participate in bonding and electronic delocalization to enhance the electronic conductivity and stabilize the materials. The powder X-ray diffraction (PXRD) spectrum of Nd-cMOF matches the simulated one demonstrating successful synthesis of the framework, and the peaks at 4.6°, 8.0°, 13.9°, and 16.2° can be indexed to the [100], [110], [211], and [202] planes of Nd-cMOF (Figure 2B), respectively. The high resolution transition electron microscopy (HRTEM) image of Nd-cMOF shows a thin film morphology with distinct lattice fringes of approximately 3.1 Å consistent with the simulated structure along the [010] plane of the crystal (Figures 2A and 2C). The electron-diffraction pattern confirms high crystallization of Nd-cMOF (Figure 2D). Four ZIFs (ZIF-1, ZIF-3, ZIF-10, ZIF-70) with pore diameters of 0.69, 0.82, 1.2, and 1.4 nm are mixed with polyacrylonitrile (PAN), respectively, to form ZIF-1-CF, ZIF-3-CF, ZIF-10-CF, and ZIF-70-CF by electrospinning.[53,54] To synthesize Nd-cMOF/ZIF-CFs, 2,3,6,7,10,11-hexaamino-triphenylene hexahydrochloride (HTPA), neodymium trichloride hexahydrate, and ZIF-derived carbon fibers are

https://doi.org/10.1021/acsami.3c04341
ACS Appl. Mater. Interfaces 2023, 15, 29170−29177

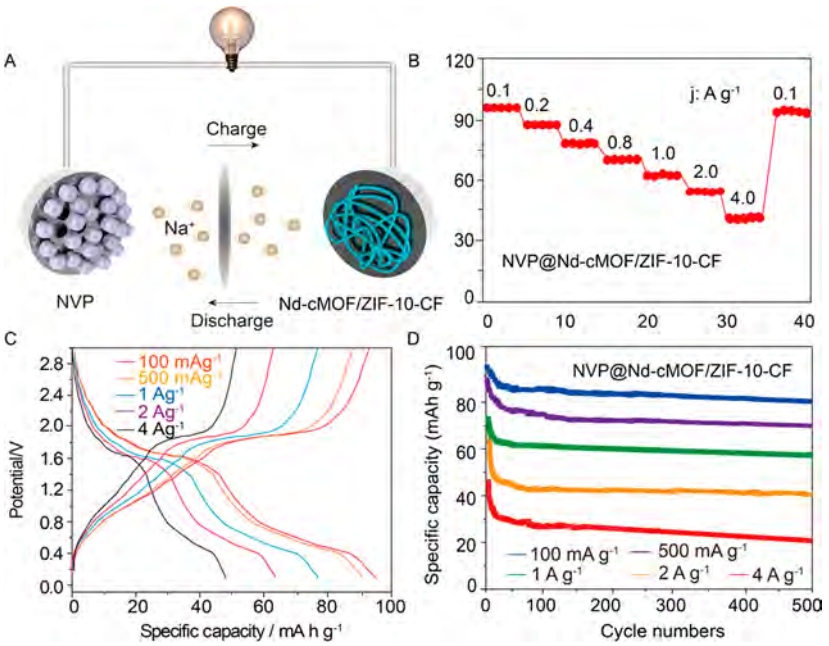

Figure 4. Electrochemical measurements of the NVP@Nd-cMOF/ZIF-10-CF full cell: (A) schematic illustration of the SIB full-cell; (B) rate capability of NVP@Nd-cMOF/ZIF-10-CF from 100 mA g^{-1} to 4 A g^{-1}; (C) initial charging−discharging curves of NVP@Nd-cMOF/ZIF-10-CF at different current densities; (D) cyclic stability of NVP@Nd-cMOF/ZIF-10-CF at different current densities.

mixed in an aqueous solution and stirred vigorously to form a homogeneous solution under ambient conditions. Triethylamine is added dropwise, capped in a Pyrex vial, and heated to 85 °C for 4 days to produce the solid product. Owing to the abundant ammonium ions in the building blocks of HTPA, the cMOF can be deposited on the ZIF-derived carbon fiber uniformly through hydrogen and $\pi-\pi$ bonds. The powder X-ray diffraction (PXRD) pattern of Nd-cMOF/ZIF-CFs matches the simulated one, corroborating successful synthesis. The peaks at 4.6°, 8.0°, 13.9°, and 16.2° can be indexed to the [100], [110], [211], and [202] planes of Nd-cMOF, and the carbon peak at 24° corresponds to the {002} plane of graphite, revealing synthesis of Nd-cMOF/ZIF-CFs (Figure 2E). SEM reveals a double-layer film on Nd-cMOF/ZIF-10-CF (Figure 2F), and the Nd-cMOF film with a thickness of 50 nm grows uniformly on the ZIF-10-CF film with a thickness of 500 nm. The ZIF-CFs appear black, and Nd-cMOF is a uniform and dense brown film (Figure 2G and Figure S9). Uniform deposition facilitates storage of Na^+ and electron transport due to the effects of voids and high mechanical strength. N_2 adsorption is investigated to evaluate the porosity of Nd-cMOF/ZIF-CFs at 77 K, and the Brunauer−Emmett−Teller (BET) area is enlarged to 470 m^2/g (Figure 2H). EDS discloses prominent peaks of Nd and N with Nd/N being 1.1:4, which is consistent with the structure of Nd-cMOF/ZIF-10-CF with an Nd/N ratio of 1:4 (Figure S10).

The electrochemical properties of CF, ZIF-10-CF, Nd-cMOF/CF, and Nd-cMOF/ZIF-10-CF at 100 mA g^{-1} are presented in Figure 3A and Figure S11. The initial discharging capacities of CF, ZIF-10-CF, Nd-cMOF/CF, and Nd-cMOF/ZIF-10-CF are 285.5, 301.5, 399.5, and 480.5 mAh g^{-1}, respectively. The Nd-cMOF/ZIF-10-CF electrode keeps a high capacity of 409 mAh g^{-1} after 500 cycles, whereas Nd-cMOF/CF only shows 335.7 mAh g^{-1} after 500 cycles, implying that Nd-cMOF/ZIF-10-CF is superior to Nd-cMOF/CF as anode material. In comparison, the electrodes of bare ZIF-10-CF and CF have low capacities of 301.2 and 251.5 mAh g^{-1}, respectively. The discharging capacities increase gradually in the order Nd-cMOF/ZIF-1-CF < Nd-cMOF/ZIF-3-CF < Nd-cMOF/ZIF-10-CF, possibly due to the different pore diameters of ZIFs. The results show that ZIF-CFs with a large pore diameter deliver better performance. However, the discharging capacity of Nd-cMOF/ZIF-70-CF is smaller than that of Nd-cMOF/ZIF-10-CF, indicating an excessively large pore diameter (pore diameter of ZIF-70 is 1.4 nm and bigger than the 1.2 nm of ZIF-10) may collapse the ZIF platform after carbonization. ZIF-10-CF has the optimal structure (Figure S12). Figure S13 shows galvanostatic discharging−charging curves of the Nd-cMOF/ZIF-10-CF electrode for different cycles at 100 mA g^{-1}. Figure S14 indicates the structural integrity of the Nd-cMOF/ZIF-10-CF electrode was retained after 500 cycles.

Figure 3B shows the rate characteristics of the four samples. The Nd-cMOF/ZIF-10-CF electrode shows specific capacities of 480.5, 395.1, 355.2, 245.5, and 165.2 mAh g^{-1} at current densities of 0.05, 0.2, 1.0, 5.0, and 10.0 A g^{-1}, respectively. A specific capacity of 468.3 mAh g^{-1} can be regained when the current is reinstall to 0.05 A g^{-1}. In comparison, the Nd-cMOF/CF electrode has specific capacities of 405.6, 304.8, 260.5, 145.5, and 101.5 mAh g^{-1} at current densities of 0.05, 0.2, 1.0, 5.0, and 10.0 A g^{-1}, respectively, and a specific capacity of 403.5 mAh g^{-1} can be retrieved when the current is reinstalled to 0.05 A g^{-1}. The rate characteristics of the blank CF and ZIF-10-CF are inferior to those of the Nd-cMOF/ZIF-10-CF electrode (Figure 3B). The results reconfirm that Nd-cMOF/ZIF-10-CF is better than CF, ZIF-10-CF, and Nd-cMOF/CF.

Figure 3C shows the first cycle of the charging/discharging curves of the four samples at 100 mA g^{-1}. The electrochemical properties of Nd-cMOF/ZIF-10-CF are better than those of CF, ZIF-10-CF, and Nd-cMOF/CF. Without the support of ZIF-10-CF, Nd-cMOF in Nd-cMOF/CF lacks the confine-

https://doi.org/10.1021/acsami.3c04341
ACS Appl. Mater. Interfaces 2023, 15, 29170−29177

ment effects of the ZIF-10-CF platform, leading to likely aggregation, pulverization, and detachment during repeated sodiation/desodiation. As for the bare CF and ZIF-10-CF electrodes, the poorer performance probably stems from the lack of interfacial active sites and voids.

Figure 3D shows the electrical conductivity of the four electrodes. The impedance plots reveal a depressed semicircle in the high-frequency region corresponding to the charge transfer process and the sloping straight line in the low-frequency region corresponds to the mass transfer process. The charge transfer resistances of CF, ZIF-10-CF, Nd-cMOF/CF, and Nd-cMOF/ZIF-10-CF are 62 Ω, 58 Ω, 45 Ω, and 21 Ω, respectively. The larger conductivity confirms the advantages of of Nd-cMOF supported by ZIF-10-CF. Figure 3E,F shows the high cycling stability of Nd-cMOF/ZIF-10-CF, and Figure 3E displays the CV curve of Nd-cMOF/ZIF-10-CF in the first five cycles. In the first reduction process, the two small reduction peaks at 1.32 and 1.51 V are related to electrolyte decomposition on the different active surface sites of the electrode leading to the formation of a solid-electrolyte interphase (SEI). In the subsequent four cycles, no remarkable change can be observed, illustrating good cycling stability and reversibility. The cycling characteristics of Nd-cMOF/ZIF-10-CF at different current densities are showed in Figure 3F, which reveals retained capacities of 409, 356, 280, 220, 175, and 102 mA h g^{-1} at current densities of 100 mA g^{-1}, 500 mA g^{-1}, 1 A g^{-1}, 3 A g^{-1}, 5 A g^{-1}, and 10 A g^{-1} after 500 charging−discharging cycles, thereby concretely demonstrating the high capacity and superior cycling stability.

Owing to the superior properties of the Nd-cMOF/ZIF-10-CF electrode in the half-cell, the NVP@Nd-cMOF/ZIF-10-CF full cell is assembled with the NVP cathode and Nd-cMOF/ZIF-10-CF anode to assess the full-cell electrochemical performance and practicability (Figure 4A). The rate graphs from 0.1 to 4 A g^{-1} show that the specific capacity at 0.1 A g^{-1} is about 93 mA h g^{-1}, and at a high rate of 4 A g^{-1}, the cell still possesses a capacity of 23 mA h g^{-1} (Figure 4B). Figure 4C shows the initial charging and discharging curves of the NVP@Nd-cMOF/ZIF-10-CF full cell at different current densities in the voltage range of 0−3.0 V. The active mass loadings of the cathode and anode are 3−4 and 1−2 mg cm^{-2}. The cycling characteristics of NVP@Nd-cMOF/ZIF-10-CF at different current densities in Figure 4D show that the retained capacities are 86.1, 72.3, 62.3, 41.3, and 23.5 mA h g^{-1} at current densities of 100 mA g^{-1}, 500 mA g^{-1}, 1 A g^{-1}, 2 A g^{-1}, and 4 A g^{-1} after 500 charging−discharging cycles, corroborating the high capacity and superior cycling stability. The negative/positive capacity ratio (N/P ratio) is 1.03, and the inset in the figure shows that one coin-type full cell can power the bulbs adequately.

CONCLUSION

Nd-cMOF is prepared *in situ* on porous carbon with the ZIF precursors, and different structures of Nd-cMOF/ZIF-CFs are fabricated to assess the conductivity and other properties. As anodes in sodium-ion batteries, the materials show outstanding capacity, long cycling stability, and excellent rate characteristics. For example, Nd-cMOF/ZIF-10-CF has a reversible capacity of 409 mAh g^{-1} at a current density of 0.1 A g^{-1} after 500 cycles. The excellent sodium storage properties of the Nd-cMOF/ZIF-10-CF electrode can be attributed to the combined effects of Nd-cMOF and ZIF-10-CF platform. ZIF-10-CF provides the electroconductivity, flexible porous structure, and mechanical stability, while Nd-cMOF provides the interfacial kinetic activity, electroconductivity, ample space, as well as volume buffer. The results provide insights into the design and preparation of progressive anode materials for sodium-ion batteries.

ASSOCIATED CONTENT

Supporting Information

The Supporting Information is available free of charge at https://pubs.acs.org/doi/10.1021/acsami.3c04341.

Picture and molecular formula of Nd-cMOF; PXRD of ZIFs; topological structure of ZIFs; synthetic strategy of ZIF-CF; spun membranes of ZIFs; image and EDS spectra of Nd-cMOF/ZIF-10-CF; images of Nd-cMOF/ZIF-CFs; electrochemical test of Nd-MOF/ZIF-CFs; PXRD of Nd-cMOF/ZIF-10-CF for precycle and after 500 cycles; discharge−charge curves of Nd-cMOF/ZIF-CFs; diffusion coefficient of sodium ions of electrode materials; galvanostatic charging−discharging curves of NVP (PDF)

AUTHOR INFORMATION

Corresponding Authors

Yue Xu − *State Key Laboratory of Material Processing and Die & Mould Technology, School of Materials Science and Engineering, Huazhong University of Science and Technology, Wuhan, Hubei 430074, China; Department of Physics, Department of Materials Science and Engineering, and Department of Biomedical Engineering, City University of Hong Kong, Kowloon, Hong Kong, China;* orcid.org/0000-0002-4677-5173; Email: xuyue@hust.edu.cn

Chun Fang − *State Key Laboratory of Material Processing and Die & Mould Technology, School of Materials Science and Engineering, Huazhong University of Science and Technology, Wuhan, Hubei 430074, China;* orcid.org/0000-0002-6511-1524; Email: fangchun@hust.edu.cn

Authors

Hongmei Dai − *State Key Laboratory of Material Processing and Die & Mould Technology, School of Materials Science and Engineering, Huazhong University of Science and Technology, Wuhan, Hubei 430074, China;* orcid.org/0000-0002-4056-8915

Yongchao Han − *State Key Laboratory of Material Processing and Die & Mould Technology, School of Materials Science and Engineering, Huazhong University of Science and Technology, Wuhan, Hubei 430074, China*

Shixiong Sun − *State Key Laboratory of Material Processing and Die & Mould Technology, School of Materials Science and Engineering, Huazhong University of Science and Technology, Wuhan, Hubei 430074, China*

Xiaolin Zhang − *Department of Physics, Department of Materials Science and Engineering, and Department of Biomedical Engineering, City University of Hong Kong, Kowloon, Hong Kong, China*

Fangyu Xiong − *Department of Physics, Department of Materials Science and Engineering, and Department of Biomedical Engineering, City University of Hong Kong, Kowloon, Hong Kong, China*

Chao Huang − *Department of Physics, Department of Materials Science and Engineering, and Department of*

Biomedical Engineering, City University of Hong Kong, Kowloon, Hong Kong, China

Jiantao Han − *State Key Laboratory of Material Processing and Die & Mould Technology, School of Materials Science and Engineering, Huazhong University of Science and Technology, Wuhan, Hubei 430074, China;* orcid.org/0000-0002-9509-3785

Paul K. Chu − *Department of Physics, Department of Materials Science and Engineering, and Department of Biomedical Engineering, City University of Hong Kong, Kowloon, Hong Kong, China;* orcid.org/0000-0002-5581-4883

Complete contact information is available at: https://pubs.acs.org/10.1021/acsami.3c04341

Notes

The authors declare no competing financial interest.

■ ACKNOWLEDGMENTS

This reseach was jointly supported by the National NSFC Nos. 51732005, 52172201, 51902118, and 52102249; international postdoctoral exchange fellowship program No. PC2021026; Postdoctoral Science Foundation of China Nos. 2019M662609, 2020T130217, and 2022M721228; City University of Hong Kong Donation Research Grant No. 9229021; City University of Hong Kong SRG No. 7005505; and City University of Hong Kong Donation Grant No. 9220061.

■ REFERENCES

(1) Liang, Y. R.; Lai, W. H.; Miao, Z. C.; Chou, S. L. Nanocomposite Materials for the Sodium-Ion Battery: A Review. *Small* **2018**, *14*, 1702514−1702534.

(2) Chayambuka, K.; Mulder, G.; Danilov, D. L.; Notten, P. H. L. Sodium-Ion Battery Materials and Electrochemical Properties Reviewed. *Adv. Energy Mater.* **2018**, *8*, 1800079.

(3) Shadike, Z.; Zhao, E. Y.; Zhou, Y. N.; Yu, X. Q.; Yang, Y.; Hu, E. Y.; Seongmin, B.; Gu, L.; Yang, X. Q. Advanced Characterization Techniques for Sodium-Ion Battery Studies. *Adv. Energy Mater.* **2018**, *8*, 1702588−1702617.

(4) Deng, J. Q.; Luo, W. B.; Chou, S. L.; Liu, H. K.; Dou, S. X. Sodium-Ion Batteries: From Academic Research to Practical Commercialization. *Adv. Energy Mater.* **2018**, *8*, 1701428−1701445.

(5) Mao, J. F.; Zhou, T. F.; Zheng, Y.; Gao, H.; Liu, H. K.; Guo, Z. P. Two-dimensional Nanostructures for Sodium-ion Battery anodes. *J. Mater. Chem. A* **2018**, *6*, 3284−3303.

(6) Zhang, Y.; Xia, X. H.; Liu, B.; Deng, S. J.; Xie, T.; Liu, Q.; Wang, Y. D.; Wu, J. B.; Wang, X. L.; Tu, J. P. Multiscale Graphene-Based Materials for Applications in Sodium Ion Batteries. *Adv. Energy Mater.* **2019**, *9*, 1803342−1803377.

(7) Liu, M. K.; Zhang, P.; Qu, Z. H.; Yan, Y.; Lai, C.; Liu, T. X.; Zhang, S. Q. Conductive Carbon Nanofiber Interpenetratedgraphene Architecture for Ultra-Stable Sodiumion Battery. *Nat.Commu.* **2019**, *10*, 3971−3988.

(8) Lu, Y.; Lu, Y. Y.; Niu, Z. Q.; Chen, J. Graphene-Based Nanomaterials for Sodium-Ion Batteries. *Adv. Energy Mater.* **2018**, *8*, 1702469−1702490.

(9) Chen, W. H.; Zhang, X. X.; Mi, L. W.; Liu, C. T.; Zhang, J. M.; Cui, S. Z.; Feng, X. M.; Cao, Y. L.; Shen, C. Y. High-Performance Flexible Freestanding Anode with Hierarchical 3D Carbon-Networks/Fe_7S_8/Graphene for Applicable Sodium-Ion Batteries. *Adv. Mater.* **2019**, *31*, 1806664−1806673.

(10) Wang, L.; Wei, Z. X.; Mao, M. L.; Wang, H. X.; Li, Y. T.; Ma, J. M. Metal Oxide/Graphene Composite Anode Materials for Sodium-Ion Batteries. *Energy Storage Materials* **2019**, *16*, 434−454.

(11) Yan, R. Y.; Josef, E.; Huang, H. J.; Leus, H.; Niederberger, M.; Hofmann, J. P.; Walczak, R.; Antonietti, M.; Oschatz, M. Understanding the Charge Storage Mechanism to Achieve High Capacity and Fast Ion Storage in Sodium-Ion Capacitor Anodes by Using Electrospun Nitrogen-Doped Carbon Fibers. *Adv. Funct. Mater.* **2019**, *29*, 1902858−1902871.

(12) Chen, Q.; Sun, S.; Zhai, T.; Yang, M.; Zhao, X. Y.; Xia, H. Yolk-Shell NiS_2 Nanoparticle-Embedded Carbon Fibers for Flexible Fiber-Shaped Sodium Battery. *Adv. Energy Mater.* **2018**, *8*, 1800054−1800063.

(13) Xiong, P. X.; Bai, P. X.; Tu, S. B.; Cheng, M.; Zhang, J. F.; Sun, J.; Xu, Y. H. Red Phosphorus Nanoparticle@3D Interconnected Carbon Nanosheet Framework Composite for Potassium-Ion Battery Anodes. *Nana. Micro Small* **2018**, *14*, 1802140−1802149.

(14) Zhang, S.; Yu, X. B.; Yu, H. L.; Chen, Y. J.; Gao, P.; Li, C. Y.; Zhu, C. L. Growth of Ultrathin MoS_2 Nanosheets with Expanded Spacing of (002) Plane on Carbon Nanotubes for High-Performance Sodium-Ion Battery Anodes. *ACS Appl. Mater. Interfaces* **2014**, *6*, 21880−21885.

(15) Zhang, Y.; Xia, X. H.; Liu, B.; Deng, S. J.; Xie, D.; Liu, Q.; Wang, Y. D.; Wu, J. B.; Wang, X. L.; Tu, J. P. Multiscale Graphene-Based Materials for Applications in Sodium Ion Batteries. *Adv. Energy Mater.* **2019**, *9*, 1803342−1803377.

(16) Lu, P.; Sun, Y.; Xiang, H. F.; Liang, X.; Yu, Y. 3D Amorphous Carbon with Controlled Porous and Disordered Structures as a High-Rate Anode Material for Sodium-Ion Batteries. *Adv. Energy Mater.* **2018**, *8*, 1702434−1702442.

(17) Yang, H.; Xu, R.; Gong, Y.; Yao, Y.; Gu, L.; Yu, Y. An Interpenetrating 3D Porous Reticular Nb_2O_5@Carbon Thin Film for Superior Sodium Storage. *Nano Energy* **2018**, *48*, 448−455.

(18) Tan, H. T.; Chen, D.; Rui, X. H.; YU, Y. Peering into Alloy Anodes for Sodium-Ion Batteries: Current Trends, Challenges, and Opportunities. *Adv. Funct. Mater.* **2019**, *29*, 1808745−1808777.

(19) Kalisvaart, W. P.; Olsen, B. C.; Luber, E. J.; Buriak, J. M. Sb-Si Alloys and Multilayers for Sodium Ion Battery Anodes. *ACS Appl. Energy Mater.* **2019**, *2*, 2205−2213.

(20) Ying, H.; Han, W. Q. Metallic Sn-Based Anode Materials: Application in High-Performance Lithium-Ion and Sodium-Ion Batteries. *Adv. Sci.* **2017**, *4*, 1700298−1700308.

(21) Wang, L. G.; Wang, J. J.; Guo, F. M.; Ma, L.; Ren, Y.; Wu, T. P.; Zuo, P. J.; Yin, G. P.; Wang, J. Understanding the Initial Irreversibility of Metal Sulfides for Sodium-Ion Batteries via Operando Techniques. *Nano Energy* **2018**, *43*, 184−191.

(22) Fang, G. Z.; Wu, Z. X.; Zhou, J.; Zhu, C. Y.; Cao, X. X.; Lin, T. Q.; Chen, Y. M.; Wang, C.; Pan, A. Q.; Liang, S. Q. Observation of Pseudocapacitive Effect and Fast Ion Diffusion in Bimetallic Sulfides as an Advanced Sodium-Ion Battery Anode. *Adv. Energy Mater.* **2018**, *8*, 1703155−1703165.

(23) Zhao, Y.; Wang, L. P.; Sougrati, M. T.; Feng, Z. X.; Leconte, Y.; Fisher, A.; Srinivasan, M.; Xu, Z. C. A Review on Design Strategies for Carbon Based Metal Oxides and Sulfides Nanocomposites for High Performance Li and Na Ion Battery Anodes. *Adv. Energy Mater.* **2017**, *7*, 1601424−1601429.

(24) Saddique, J.; Zhang, X.; Wu, T. H.; Wang, X.; Chen, X. P.; Su, H.; Liu, S. Q.; Zhang, L. Q.; Li, G. Y.; Zhang, Y. F.; Yu, H. J. Enhanced Silicon Diphosphide-Carbon Composite Anode for Long-Cycle, High-Efficient Sodium Ion Batteries. *ACS Appl. Energy Mater.* **2019**, *2*, 2223−2229.

(25) Li, P.; Hwang, J.-Y.; Sun, Y.-K. Nano/Micro-Structured Silicon-Graphite Composite Anode for High-Energy Density Li-Ion Battery. *ACS Nano* **2019**, *13*, 2624−2633.

(26) Lu, H. Y.; Ai, F. X.; Jia, Y. L.; Tang, C. Y.; Zhang, X. H.; Huang, Y. H.; Yang, H. X.; Cao, Y. L. Exploring Sodium-Ion Storage Mechanism in Hard Carbons with Different Microstructure Prepared by Ball-Milling Method. *Small* **2018**, *14*, 1802694−1802702.

(27) Sun, N.; Guan, Z. R.; Liu, Y. W.; Cao, Y. L.; Zhu, Q. Z.; Liu, H.; Wang, Z. X.; Zhang, P.; Xu, B. Extended "Adsorption-Insertion" Model: A New Insight into the Sodium Storage Mechanism of Hard Carbons. *Adv. Energy Mater.* **2019**, *9*, 1901351−1901365.

(28) Qiu, S.; Xiao, L.; Sushko, M. L.; Han, K. S.; Shao, Y.; Yan, M.; Liang, X.; Mai, L.; Feng, J.; Cao, Y.; Ai, X.; Yang, H.; Liu, J. Manipulating Adsorption-Insertion Mechanisms in Nanostructured Carbon Materials for High-Efficiency Sodium Ion Storage. *Adv. Energy Mater.* **2017**, *7*, 1700403−1700508.
(29) Marti, A.; Venna, S.; Roth, E. A.; Culp, J. T.; Hopkinson, D. P. A Simple Fabrication Method for Mixed Matrix Membranes with In-siut MOF Growth for Gas Separation. *ACS Appl. Mater. Interfaces* **2018**, *10*, 24784−24790.
(30) Gu, J.; Fan, H.; Li, C.; Caro, J.; Meng, H. Robust Superhydrophobic/Superoleophilic Wrinkled Microspherical MOF@rGO Composites for Efficient Oil-Water Separation. *Angew. Chem.* **2019**, *131*, 5351−5355.
(31) Ren, J.; Huang, Y.; Zhu, H.; Zhang, B.; Zhu, H.; Shen, S.; Tan, G.; Wu, F.; He, H.; Lan, S.; Xia, X.; Liu, Q. Recent Progress on MOF-derived Carbon Materials for Energy Storage. *Carbon Energy* **2020**, *2*, 176−202.
(32) Li, Y.; Xu, Y.; Yang, W.; Shen, W.; Xue, H.; Pang, H. MOF-Derived Metal Oxide Composites for Advanced Electrochemical Energy Storage. *Small* **2018**, *14*, 1704435−1704459.
(33) Liu, Y.; Xie, X. Y.; Cheng, C.; Shao, Z. S.; Wang, H. S. Strategies to Fabricate Metal-organic Framework (MOF)-based Luminescent Sensing Platforms. *J. Mater. Chem. C* **2019**, *7*, 10743−10763.
(34) Yao, D. M.; Xiu, J. W.; Huang, Q. Q.; Li, W. H.; Wu, D. W.; Wu, A. Q.; Cao, L. A.; Deng, W. H.; Wang, D. G.; Xu, P. G. Van der Waals Heterostructured MOF-on-MOF Thin Films: Cascading Functionality to Realize Advanced Chemiresistive Sensing. *Angew. Chem., Int. Ed.* **2019**, *58*, 14915−14919.
(35) Mon, M.; Bruno, R.; Ferrando, S. J.; Bartella, L.; Donna, L. D.; Talia, M.; Lappano, R.; Maggiolini, M.; Armentano, D.; Pardo, E. Crystallographic Snapshots of the Host-Guest Interactions on Drugs@Metal-Organic Frameworks: Towards Mimicking Molecular Recognition Processes. *Mater. Horiz.* **2018**, *5*, 683−690.
(36) Kusaka, S.; Kiyose, A.; Sato, H.; Hijikata, Y.; Hori, A.; Ma, Y.; Matsuda, R. Dynamic Topochemical Reaction Tuned by Guest Molecules in the Nanospace of a Metal-Organic Framework. *J. Am. Chem. Soc.* **2019**, *141*, 15742−15746.
(37) Park, J.; Hinckley, C. A.; Huang, Z.; Feng, D.; Yakovenko, A. A.; Lee, M.; Chen, S.; Zou, X.; Bao, Z. Synthetic Routes for a 2D Semiconductive Copper Hexahydroxybenzene Metal-Organic Framework. *J. Am. Chem. Soc.* **2018**, *140*, 14533−14537.
(38) Xie, L. S.; Skorupskii, G.; Dincă, M. Electrically Conductive Metal-Organic Frameworks. *Chem. Rev.* **2020**, *120*, 8536−8580.
(39) Cai, D.; Lu, M.; Li, L.; Cao, J.; Chen, D.; Tu, H.; Li, J.; Han, W. A Highly Conductive MOF of Graphene Analogue $Ni_3(HITP)_2$ as a Sulfur Host for High-Performance Lithium-Sulfur Batteries. *Small* **2019**, *15*, 1902605−1902613.
(40) Yang, W. P.; Li, X. X.; Li, Y.; Zhu, R. M.; Pang, H. Applications of Metal-Organic-Framework-Derived Carbon Materials. *Adv. Mater.* **2018**, *31*, 1804740−1804775.
(41) Li, B.; Gu, X. J.; Jin, P. Overlooked Effects of La-4f Orbitals in Endohedral Metallofullerenes. *Inorg. Chem.* **2022**, *61*, 5891−5902.
(42) Lu, E.; Sajjad, S.; Berryman, E. V.; Wooles, J. A.; Kaltsoyannis, N.; Liddle, T. S. Emergence of the Structure-directing Role of f-orbital Overlap-driven Covalency. *Nat. Commun.* **2019**, *10*, 634−641.
(43) Zanella, S. B.; Jones, B. S.; Lee, H.; Hancock, D. R. Evidence for Participation of 4f and 5d Orbitals in Lanthanide Metal-Ligand Bonding and That Y(III) Has Less of This Complex-Stabilizing Ability. A Thermodynamic, Spectroscopic, and DFT Study of Their Complexation by the Nitrogen Donor Ligand TPEN. *Inorg. Chem.* **2022**, *61*, 4627−4638.
(44) Giannakis, I.; Leshen, J.; Kavai, M.; Ran, S.; Kang, C.; Saha, R. S.; Zhao, Y.; Xu, Z.; Lynn, W. J.; Miao, L.; Wray, A. L.; Kotliar, G.; Butch, P. N.; Aynajian, P. Orbital-selective Kondo Lattice and Enigmatic f Electrons Emerging from Inside the Antiferromagnetic Phase of a Heavy Fermion. *Sci. Adv.* **2019**, *5*, 9061−9078.
(45) Ravichandran, L.; Banik, S. Investigation of the Failure of the MP2Method to Describe the Out-of-Plane Bending Motions of Carbon-Carbon Double-Bonded Molecules: The Role of Atomic Orbitals. *J. Phys. Chem. A* **2021**, *125*, 9298−9317.
(46) Lee, J.; Ohba, N.; Asahi, R. First-principles Prediction of High Oxygen-ion Conductivity in Trilanthanide Gallates Ln_3GaO_6. *Sci. Technol. Adv. Mater.* **2019**, *20*, 144−159.
(47) Glante, S.; Hartmann, M. The Solvent and Zinc Source Dual-induced Synthesis of a Two Dimensional Zeolitic Imidazolate Framework with a Farfalle-shape and its crystal Transformation to Zeolitic Imidazolate Framework-8. *Dalton Trans.* **2021**, *50*, 398−400.
(48) Gomar, M.; Yeganegi, S. Adsorption of 5-Fluorouracil and Thioguanine Drugs into ZIF-1, ZIF-3 and ZIF-6 by Dimulation Methods. *Mater. Sci. and Eng.: C* **2019**, *97*, 461−466.
(49) Park, K. S.; Ni, Z.; Cote, A. P.; Choi, J. Y.; Huang, R.; Uribe-Romo, F. J.; Chae, H. K.; O'Keeffe, M.; Yaghi, O. M. Exceptional Chemical and Thermal Stability of Zeolitic Imidazolate Frameworks. *Proc. Natl. Acad. Sci. U.S.A.* **2006**, *103*, 10186−10191.
(50) Banerjee, R.; Furukawa, H.; Britt, D.; Knobler, C.; O'Keeffe, M.; Yaghi, O. M. Control of Pore Size and Functionality in Isoreticular Zeolitic Imidazolate Frameworks and their Carbon Dioxide Selective Capture Properties. *J. Am. Chem. Soc.* **2009**, *131*, 3875−3877.
(51) Dou, Y. B.; Zhang, W. J.; Kaiser, A. Electrospinning of Metal-Organic Frameworks for Energy and Environmental Applications. *Adv. Sci.* **2020**, *7*, 1902590−1902601.
(52) Sheberla, D.; Sun, L.; Blood-Forsythe, A. M.; Er, S.; Wade, R. C.; Brozek, K. C.; Aspuru-Guzik, A.; Dincă, M. High Electrical Conductivity in Ni_3(2,3,6,7,10,11-hexaiminotriphenylene)$_2$, a Semiconducting Metal-Organic Graphene Analogue. *J. Am. Chem. Soc.* **2014**, *25* (136), 8859−8862.
(53) Li, Y.; Zhu, J.; Cheng, H.; Li, G. Q.; Cho, H.; Jiang, M. J.; Gao, Q.; Zhang, X. W. Developments of Advanced Electrospinning Techniques: A Critical Review. *Adv. Mater. Technol.* **2021**, *6*, 2100410−2100439.
(54) Xiao, W.; Cheng, D.; Huang, L.; Song, J.; Yang, Z. X.; Qiao, Q. D. An Integrated Separator/Anode Assembly Based on Electrospinning Technique for Advanced Lithium-ion Batteries. *Electrochimi. Acta* **2021**, *389*, 138776−1387715.

https://doi.org/10.1021/acsami.3c04341
ACS Appl. Mater. Interfaces 2023, 15, 29170−29177

Supporting Information

Conductive MOF on ZIF-derived Carbon Fibers as Superior Anode in Sodium-Ion Battery

Hongmei Dai[a], Yue Xu[*a, b], Yongchao Han[a], Shixiong Sun[a], Xiaolin Zhang[b], Fangyu Xiong[b], Chao Huang[b], Chun Fang[*a], Jiantao Han[a], and Paul K. Chu[b]

[a] State Key Laboratory of Material Processing and Die & Mould Technology, School of Materials Science and Engineering, Huazhong University of Science and Technology, Wuhan, Hubei, 430074, China

[b] Department of Physics, Department of Materials Science and Engineering, and Department of Biomedical Engineering, City University of Hong Kong, Tat Chee Avenue, Kowloon, Hong Kong, China

*Corresponding authors:

E-mail: fangchun@hust.edu.cn; xuyue@hust.edu.cn

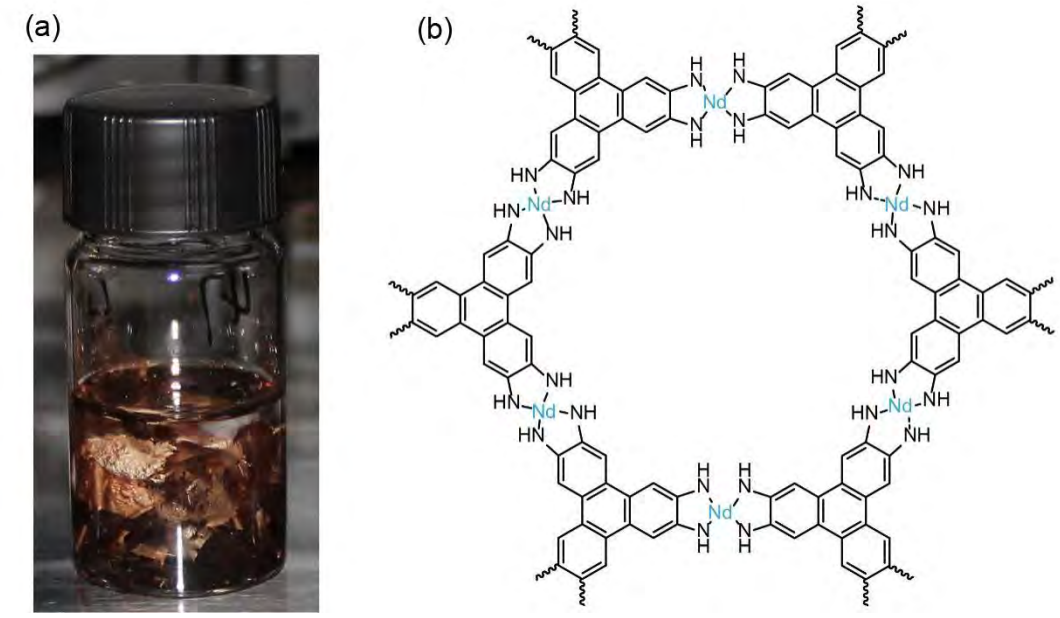

Figure S1. (a) Picture of the synthesized Nd-cMOF and (b) Molecular formula of Nd-cMOF.

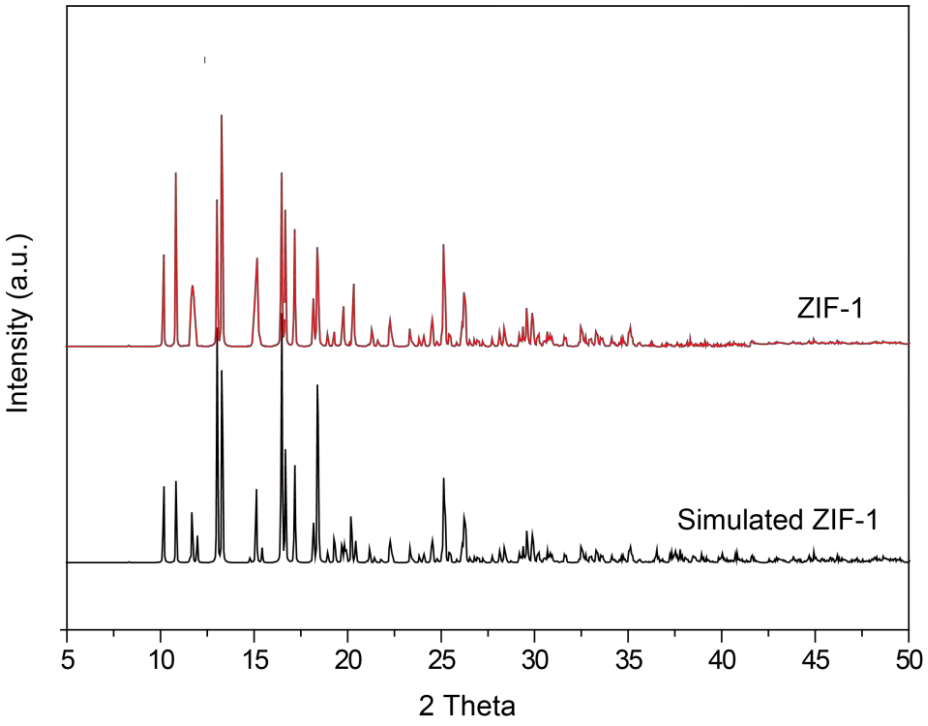

Figure S2. PXRD of as prepared ZIF-1 (red) and simulated ZIF-1(black)[1].

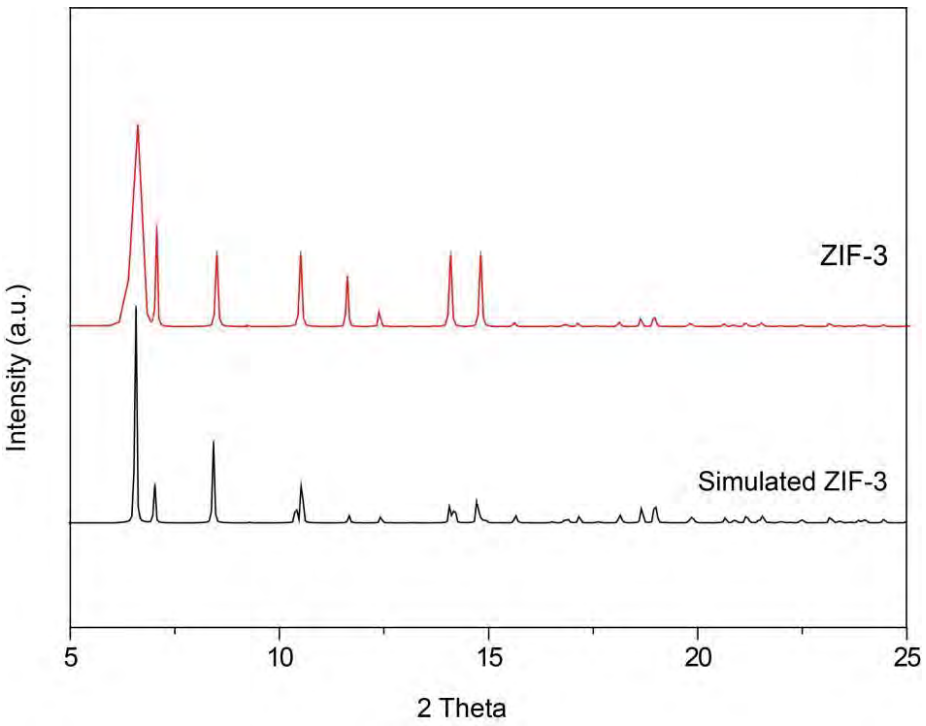

Figure S3. PXRD of ZIF-3 (red) and simulated ZIF-3 (black)[2].

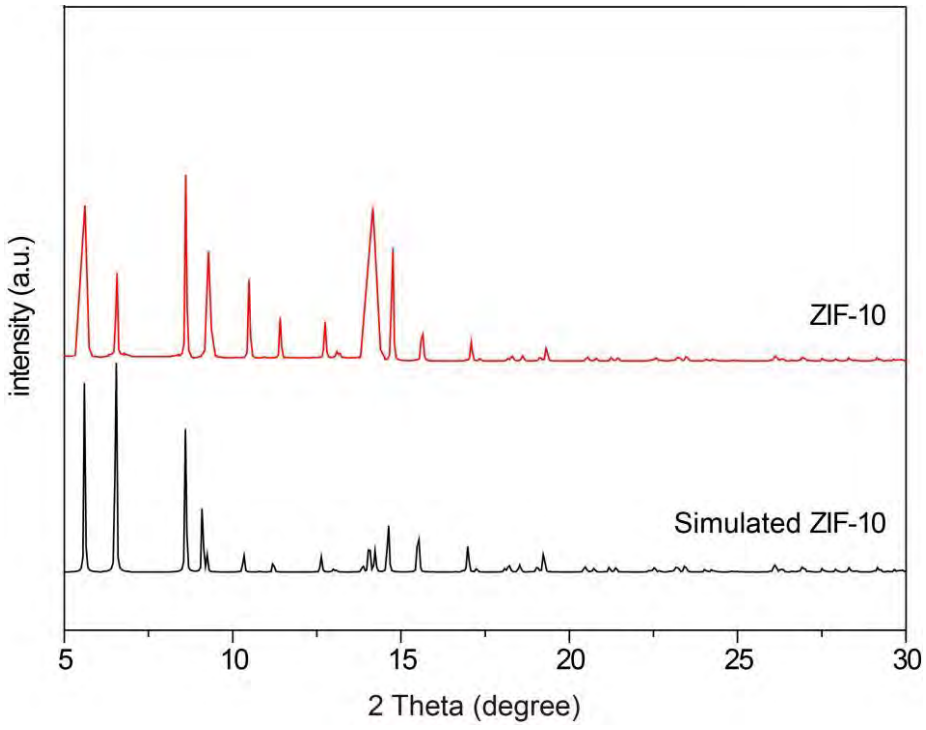

Figure S4. PXRD of ZIF-10 (red) and simulated ZIF-10 (black)[3-5].

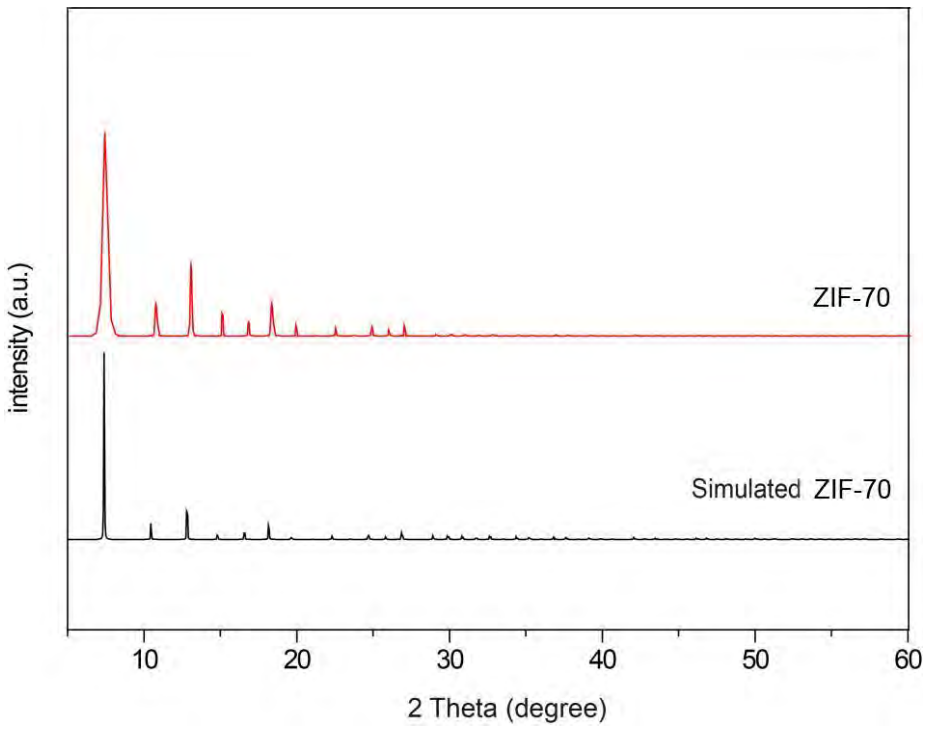

Figure S5. PXRD of as ZIF-70 (red) and simulated ZIF-70 (black)[6].

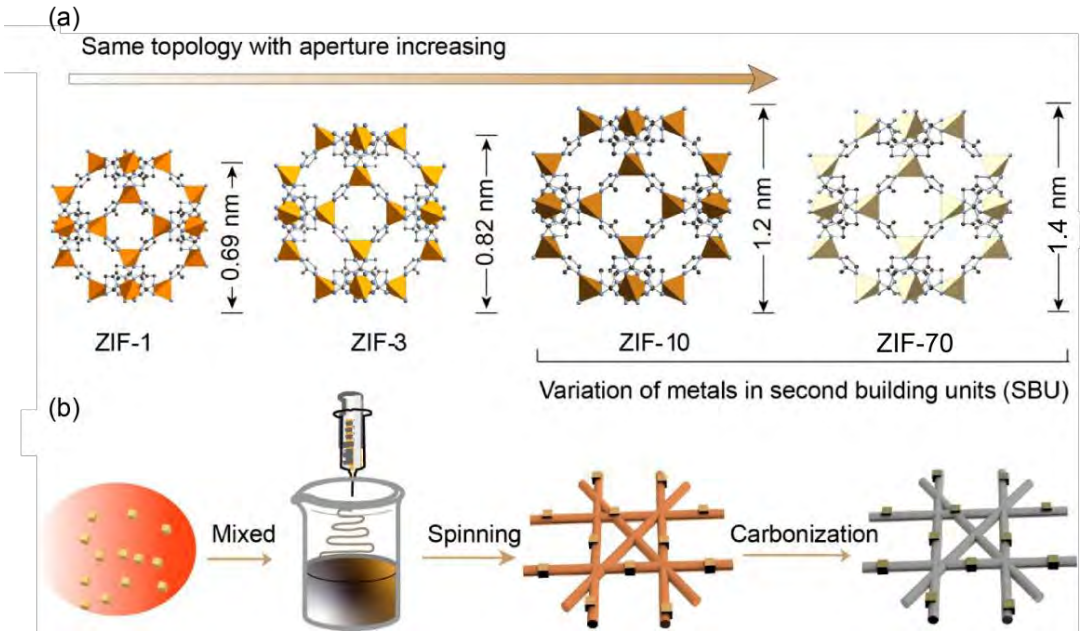

Figure S6. (a) Topological structure of ZIF-1, ZIF-3, ZIF-10 and ZIF-70 and (b) Schematic showing the synthesis of ZIF-CF by wet spinning.

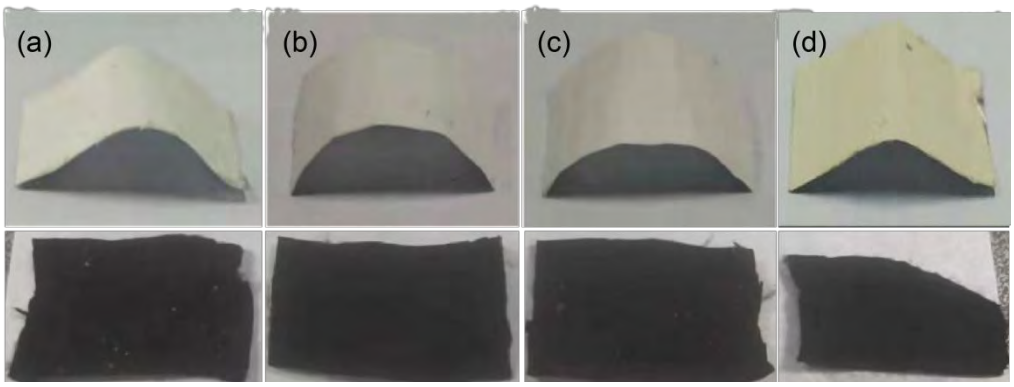

Figure S7. Spun membranes of (a) ZIF-1-CF, (b) ZIF-3-CF, (c) ZIF-10-CF, and (d) ZIF-70-CF.

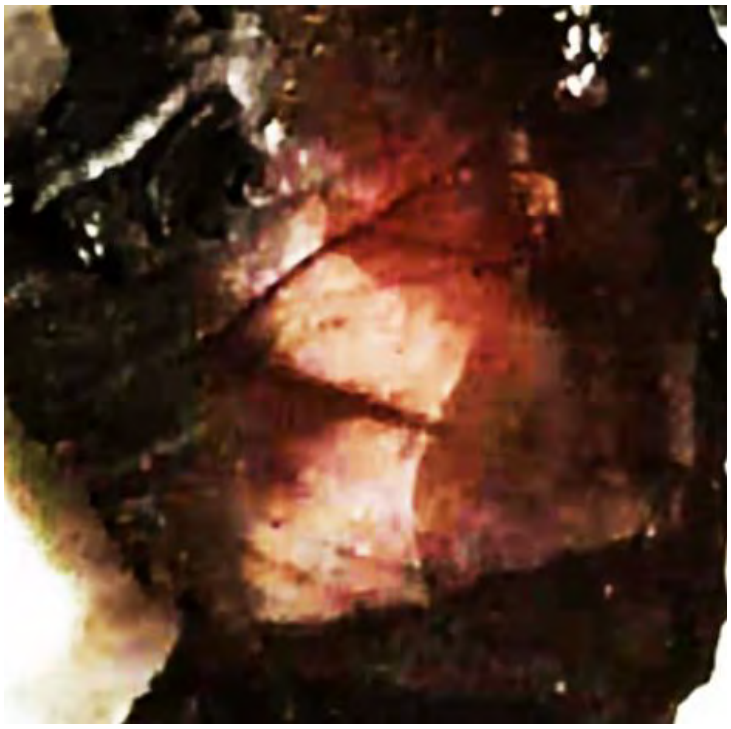

Figure S8. Image of Nd-cMOF/ZIF-10-CF.

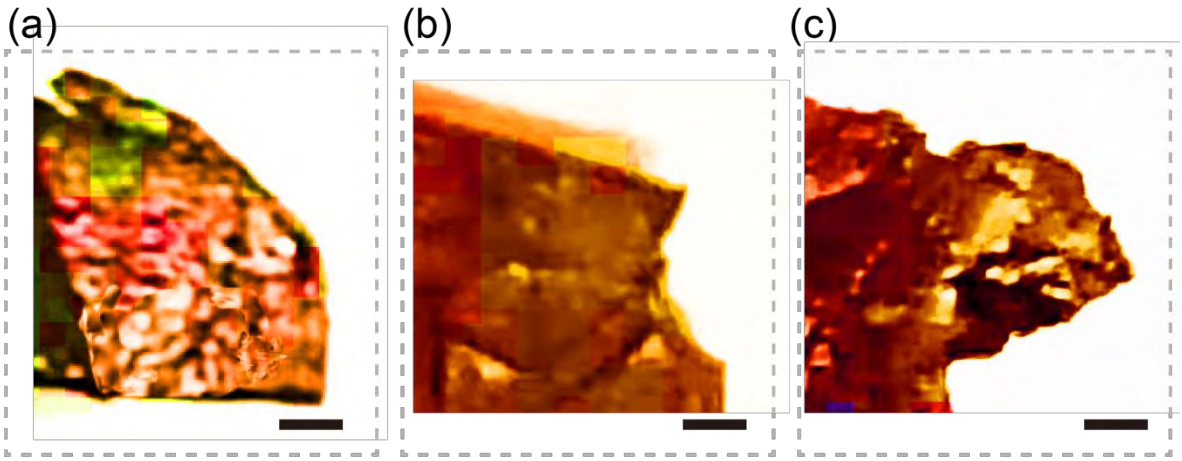

Figure S9. Images of Nd-cMOF/ZIF-1-CF(a), Nd-cMOF/ZIF-3-CF(b), Nd-cMOF/ZIF-70-CF (c). scale bar, 2 u m.

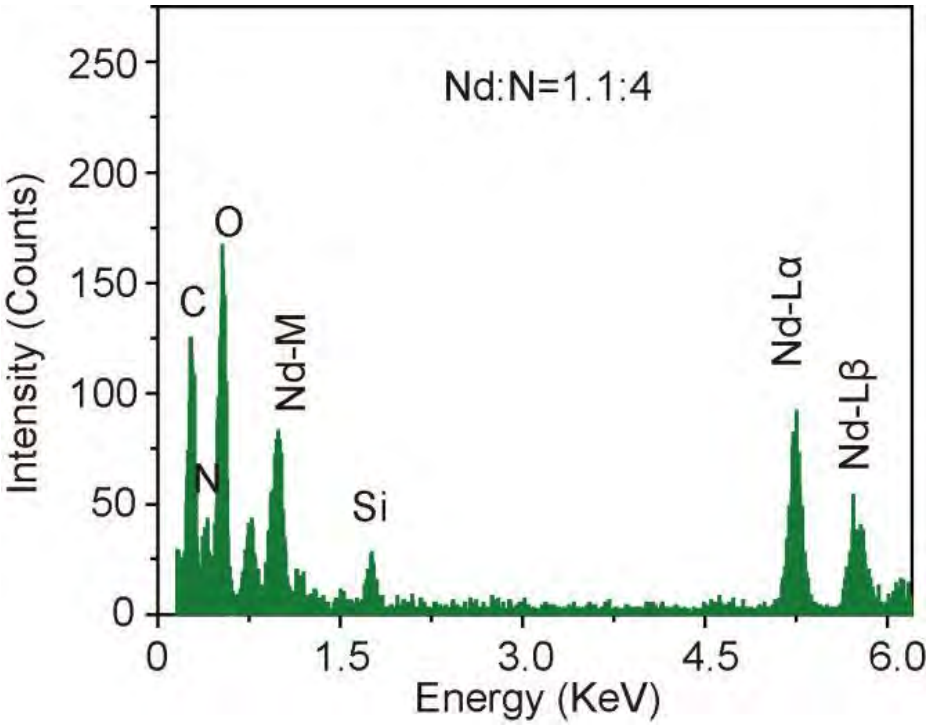

Figure S10. EDS spectra of Nd-cMOF/ZIF-10-CF.

The initial charging capacities of CF, ZIF-10, Nd-cMOF/CF, and Nd-cMOF/ZIF-10-CF are 240.1, 295.5, 385.2, and 470.5 mAh g-1, respectively. The Nd-cMOF/ZIF-10-CF electrode maintains a high capacity of 407.6 mAh g-1 after 500 cycles, whereas Nd-cMOF/CF only shows 335.1 mAh g-1 after 500 cycles, implying that Nd-cMOF/ZIF-10-CF is superior to Nd-cMOF/CF as anode materials. In comparison, the electrodes of bare ZIF-10-CF and CF have low capacities of 295.4 and 220.2 mAh g^{-1}, respectively. The charging capacities increase gradually in the order of Nd-cMOF/ZIF-1-CF < Nd-cMOF/ZIF-3-CF < Nd-cMOF/ZIF-10-CF, possibly due to the different pore diameters of ZIFs. The results showed that ZIF-10-CFs with a large pore diameter deliver better performance. However, the charging capacity of Nd-cMOF/ZIF-70-CF is lower than that of Nd-cMOF/ZIF-10-CF, indicating an excessively large pore diameter (pore diameter of ZIF-70 is 1.4 nm and bigger than 1.2 nm of ZIF-10) may collapse the ZIF platform during carbonization.

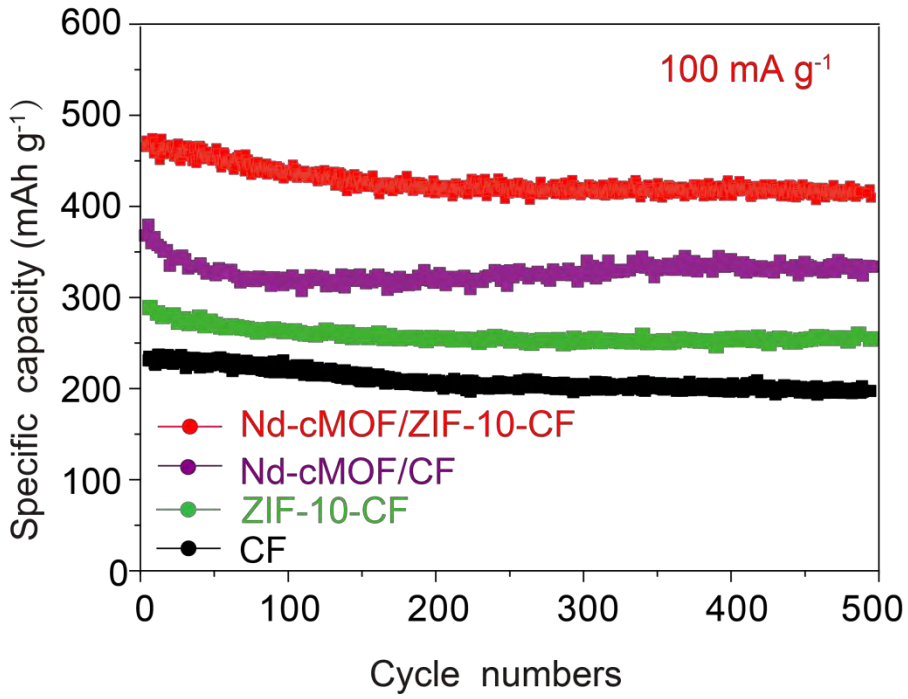

Figure S11. Cyclic stability of the Nd-cMOF/ZIF-10-CF (red), Nd-cMOF/CF (purple), ZIF-10-CF (green), and CF (black) electrodes.

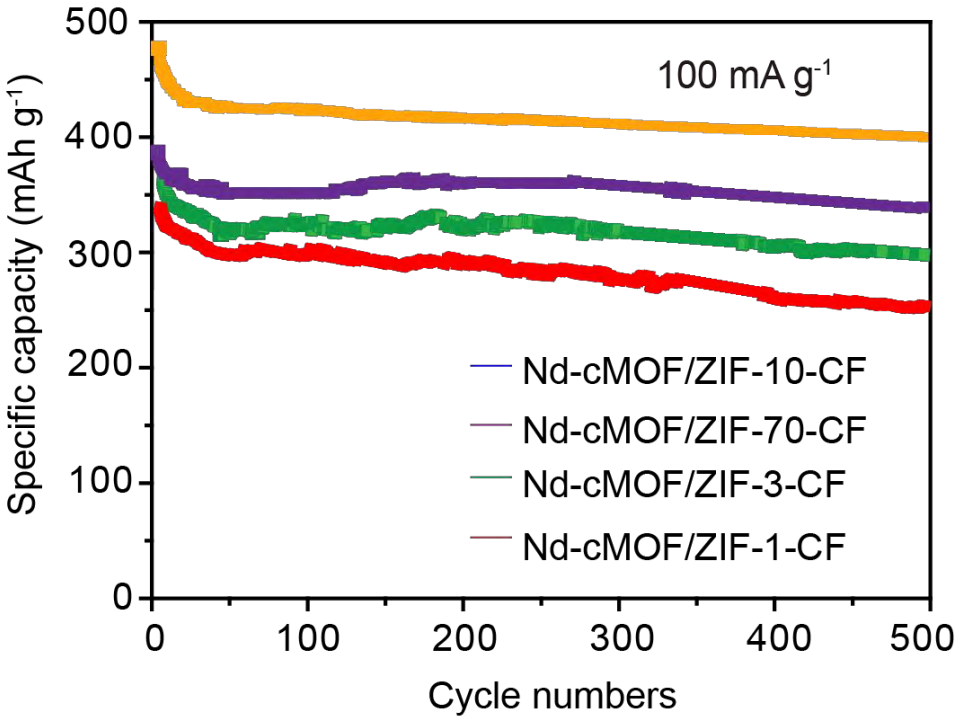

Figure S12. Cycling properties of Nd-cMOF/ZIF-10-CF (yellow), Nd-cMOF/ZIF-70-CF (purple), Nd-cMOF/ZIF-3-CF (green), and Nd-cMOF/ZIF-1-CF (red) electrodes at a current density of 100 mA g^{-1}.

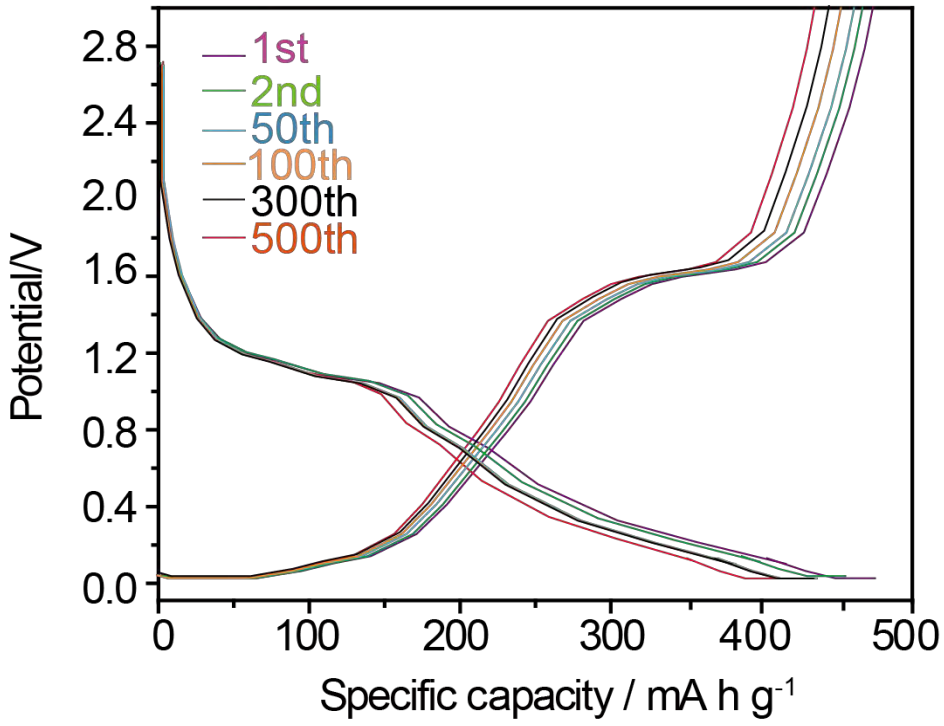

Figure S13. Galvanostatic discharging-charging curves of the Nd-cMOF/ZIF-10-CF electrode for different cycles at 100 mA g^{-1}.

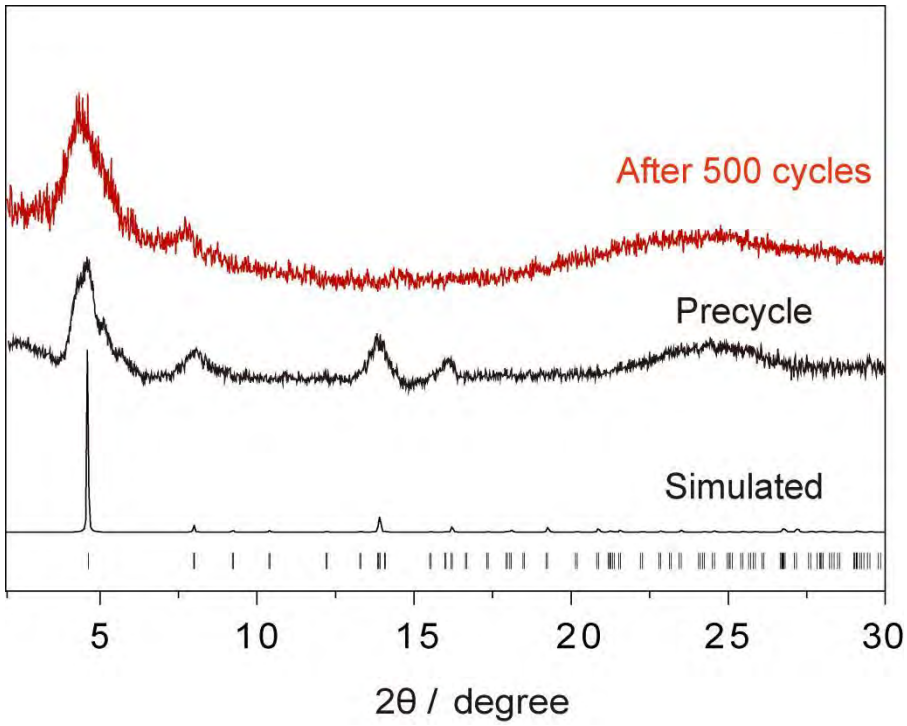

Figure S14. PXRD patterns of Nd-cMOF/ZIF-10-CF for precycle (black) and after 500 cycles (red).

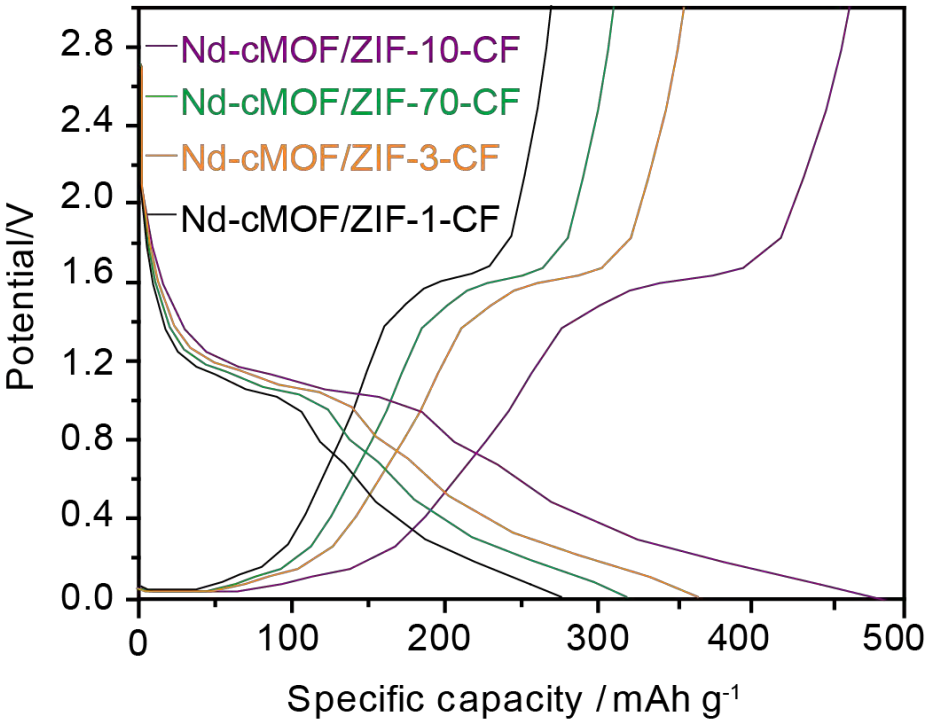

Figure S15. Discharge-charge curves of Nd-cMOF/ZIF-70-CF, Nd-cMOF/ZIF-10-CF, Nd-cMOF/ZIF-3-CF and Nd-cMOF/ZIF-1-CF electrode materials.

Diffusion coefficient of sodium ions (D_{Na}) can be obtained according to the following equations:

$$i=RT/nFRct \quad (1)$$

$$D_{Na}=R^2T^2/2A^2n^4F^4C_{Na}^2\delta^2 \quad (2)$$

where R is the gas constant, T is the absolute temperature (298.15 K), A is the surface area of the cathode (1.5 cm^{-2}), n is the number of electrons per molecule during oxidation, F is the Faraday constant, C_{Na} is the concentration of the sodium ion in the electrode, and δ is the Warburg coefficient which is related to Z':

$$Z'=R_c+R_{ct}+\delta\omega^{-1/2} \quad (3)$$

where ω is the angular frequency in the low frequency region, both R_C and Rct are kinetics parameters independent of frequency, so δ is the slope for the plot of Z' versus the reciprocal square root of the lower angular frequencies ($\omega^{-1/2}$). To obtain the Warburg coefficient (δ), the linear fitting of Z' versus $\omega^{-1/2}$ is shown in Figure S15. All the parameters are listed in Table S1.

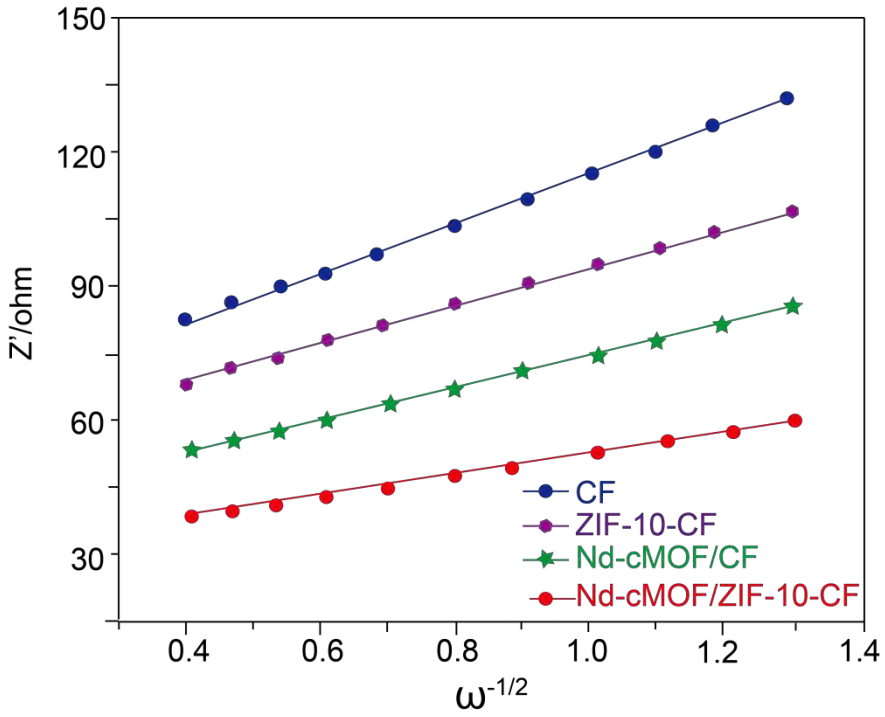

Figure S16. Relationship between Z' and $\omega^{-1/2}$ in the low frequency region of Nd-cMOF/ZIF-10-CF, Nd-cMOF/CF, ZIF-10-CF, and CF electrodes.

Table S1. EIS parameters of Nd-cMOF/ZIF-10-CF, Nd-cMOF/CF, ZIF-10-CF, and CF electrodes.

Sample	R_{ct} (Ω)	δ (Ω $s^{1/2}$)	i (mA cm^{-2})	D_{Na} (cm^2 s^{-1})
Nd-cMOF/ZIF-10-CF	21	25.21	1.18	$3.3*10^{-11}$
Nd-cMOF/CF	45	30.12	0.71	$2.1*10^{-11}$
ZIF-10-CF	58	35.24	0.46	$1.8*10^{-11}$
CF	62	42.25	0.35	$1.2*10^{-11}$

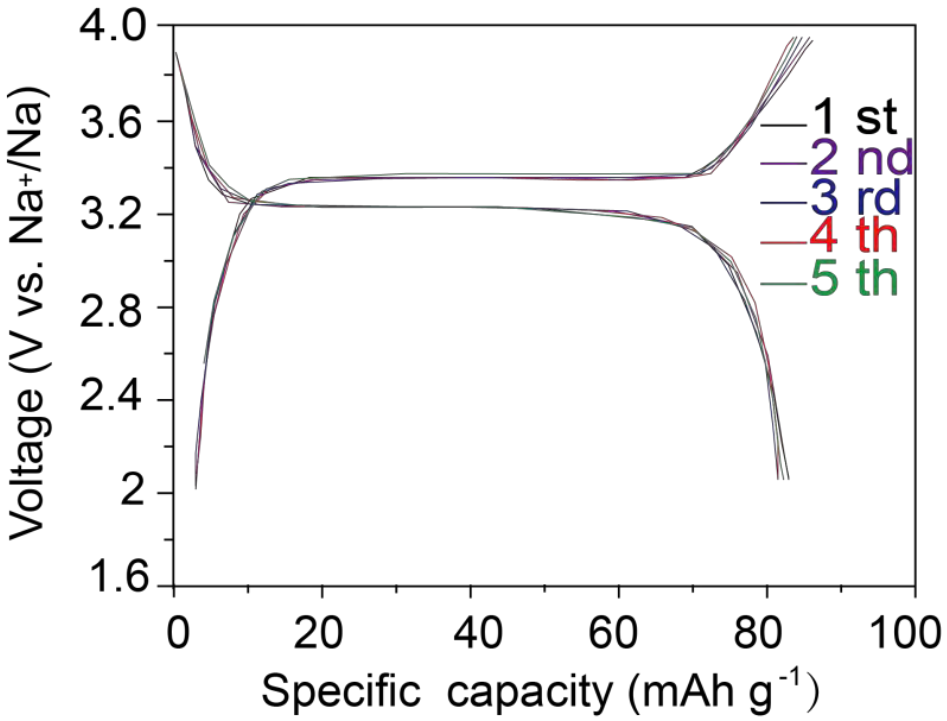

Figure S17. Galvanostatic charging-discharging curves of NVP at 1 C (1 C=117 mA g^{-1}).

References

(1) Thomas, D. B.; David, A. K.; Jin, C. T.; Emma, R. B.; Andrew, L. G.; Anthony, K. C. Thermal Amorphization of Zeolitic Imidazolate Frameworks. *Angew. Chem. Int. Ed.* **2011**, *123*, 3123-3127.

(2) Anoopa, T.; Muthuramalingam, P. Ionic Liquid Incorporation in Zeolitic Imidazolate Framework-3 for Improved CO_2 Separation: A Computational Approach. *Appl. Surf. Sci.* **2021**, *562*, 150173-150181.

(3) Gong, X. Y.; Luo, W. X.; Guo, N, N.; Zhang, S.; Wang, L. X.; Jia, D. Z.; Ai, L. L.; Feng, S. Z. Carbon Nanofiber@ZIF-8 Derived Carbon Nanosheet Composites with a Core-shell Structure Boosting Capacitive Deionization Performance. *J. Mater. Chem. A* **2021**, *9*, 18604-18613.

(4) Joseph, R.; Yang, H.; Christopher, M.; Amanda, N.; Travis. K. Reproducible Synthesis and High Porosity of mer-$Zn(Im)_2$ (ZIF-10): Exploitation of an Apparent Double-Eight Ring Template. *J. Am. Chem. Soc.* **2016**, *138*, 12017-12020.

(5) Li, L.; Zhou, G. B.; Yang, Z.; Fang, F.; Qiao, Q.; Hu, N.; Huang, L. L.; Chen, X. S. Molecular-Level Understanding of Translational and Rotational Motions of C_2H_6, C_3H_8, and n-C_4H_{10} and Their Binary Mixtures with CO_2 in ZIF-10. *J. Chem. Eng. Data* **2019**, *64*, 484-496.

(6) Rosalyn, V. K.; Thomas, P. V.; Jake, A. B.; Adam, J. M. Adsorption of Tetranitromethane in Zeolitic Imidazolate Frameworks Yields Energetic Materials. *Dalton Trans.* **2019**, *48*, 7509-7513.